Chemosphere 331 (2023) 138827

Contents lists available at ScienceDirect

Chemosphere

journal homepage: www.elsevier.com/locate/chemosphere

In situ growth of NH_2-MIL-101 metal organic frameworks on biochar for glyphosate adsorption

Qi Wang [a,b], Kang-Ping Cui [a,b,*], Tong Liu [a,b], Chen-Xuan Li [a,b], Jun Liu [c], Dian-Chao Kong [d], Rohan Weerasooriya [e], Xing Chen [a,b,e,**]

[a] *School of Resources and Environmental Engineering, Hefei University of Technology, Hefei, 230009, PR China*
[b] *Key Laboratory of Nanominerals and Pollution Control of Higher Education Institutes, Hefei University of Technology, Hefei, 230009, PR China*
[c] *Anhui Zhonghuan Environmental Protection Technology Co.,Ltd, Hefei, 230000,China*
[d] *Anhui Environmental Science and Technology Group Co. Ltd, Hefei, 230088,China*
[e] *National Centre for Water Quality Research, National Institute of Fundamental Studies, Kandy, 20000, Sri Lanka*

HIGHLIGHTS

- $NMBC_{61}$ was synthesized by in situ growing of NH_2-MIL-101 metal-organic framework on biochar through solvothermal method.
- PMG could be efficiently removed by $NMBC_{61}$.
- The PMG adsorbed on $NBMC_{61}$ via ligand exchange, electrostatic interactions and hydrogen bonding.
- No by-products were produced during the adsorption of PMG by $NMBC_{61}$.

GRAPHICAL ABSTRACT

ARTICLE INFO

Handling Editor: Yongmei Li

Keywords:
Biochar
Metal-organic framework
Functionalization
Glyphosate
Wastewater

ABSTRACT

We fabricated a novel adsorbent to remove glyphosate (PMG) in solution by in situ growing of NH_2-MIL-101 metal-organic framework on biochar derived by the calcination of waste rice husk (hereafter $NMBC_{61}$ formulated as NH_2-MIL-101: BC = 6:1 ratio). The new adsorbent was systematically characterized by atomic, molecular spectroscopic and conventional experimental methods. The PMG adsorption efficiency on $NMBC_{61}$ was examined as a function of contact time, solution pH, temperature, matrix solutes, and substrate concentration. The modification of amino group significantly improved the adsorption performance of the material. The PMG adsorption data were modeled using Langmuir isotherm and pseudo-second-order kinetics formulations. The maximum adsorption capacities of $NMBC_{61}$ at 323 K for PMG is 186.71 mg g^{-1}. The PMG adsorption did not significantly interfere with NO_3^-, Cl^-, $HCOO^-$, and citric acid in the solution matrix; SO_4^{2-} show an intermediate interfering behavior. However, PMG adsorption interferes significantly in the presence of $H_2PO_4^{2-}$ and citric acid. The contrasting interfering patterns show the nature of surface bonding in PMG adsorption on $NBMC_{61}$. The subtilties arisen between surface –NH_2 and –OH sites on PMG adsorption were resolved by IR and XPS spectral data. The PMG adsorbed on $NBMC_{61}$ via ligand exchange by inner-sphere surface complex formation. When foreign solutes show similar surface complexing, they interfere with PMG adsorption. Based on the adsorption experiments and density functional theory (DFT) calculations, the van der Waals (vdW) interactions and

---

* Corresponding author. School of Resources and Environmental Engineering, Hefei University of Technology, No. 193 Tunxi Road, Hefei, 230009, PR China.
** Corresponding author. School of Resources and Environmental Engineering, Hefei University of Technology, No. 193 Tunxi Road, Hefei, 230009, PR China.
E-mail addresses: cuikangping@hfut.edu.cn (K.-P. Cui), xingchen@hfut.edu.cn (X. Chen).

https://doi.org/10.1016/j.chemosphere.2023.138827
Received 9 February 2023; Received in revised form 14 April 2023; Accepted 29 April 2023
Available online 30 April 2023

hydrogen bonding were assumed to be involved in the adsorption. $NBMC_{61}$ shows over 83% PMG removal efficiency at the end of three cycles. The $NMBC_{61}$ show optimal PMG adsorption between pH 2 and 6 with minimal interference from the solution matrix. Therefore, $NBMC_{61}$ has the potential in treating organic pollutants found in natural and wastewaters efficiently with minimal pre-treatment steps.

1. Introduction

Glyphosate ($HOOCCH_2NHCH_2PO(OH)_2$, N- methyl phosphate glycine, solubility 10.5 g L^{-1}, specific density 1.74, log K_{ow} −3.40, K_H 2.1 x 10^{-9} P- m^3 $mole^{-1}$ and hereafter designated as PMG) is a widely used, cost-effective, and non-selective herbicide contains ionizable phosphate (pK_{a1} 2.34 at 20 °C), amino (pK_{a2} 5.73) and carboxyl (pK_{a3} 10.2) groups with a 7–60 days half-life in soils (Mesnage and Antoniou, 2017; National Library of Medicine USA viewed on 25-12-2022). Its toxicity and carcinogenic effects are debated at present (Kanissery et al., 2019). However due to its intensive use in the agriculture industry, PMG is ubiquitous in the atmosphere, hydrosphere, pedosphere, and biosphere in varying proportions (Yamaguchi et al., 2016; Mesnage and Antoniou, 2017), and therefore the development of cost-effective PMG mitigation methods is a timely need.

Current technologies in remediating PMG-polluted water bodies include adsorption (Borba et al., 2019; Hu et al., 2011; Jia et al., 2020; Xiao and Meng, 2020), biological methods (Lescano et al., 2020; Zhan et al., 2018; Singh et al., 2019), and advanced oxidation processes (Chen et al., 2007; Lv et al., 2020; Tan et al., 2019). Although high PMG removal rates can be obtained by biological methods, the process requires a long residence time and demands stringent microbial growth conditions while they do not achieve high mineralization efficiency. Advanced oxidation processes for PMG degradation are effective, but they are costly and low re-usability limits their large-scale applications. The most critical factor is both biological and advanced oxidation methods destroy PMG molecules and produce more difficult to degrade by-products (mainly aminomethylphosphonic acid (AMPA)) (Feng et al., 2020). Among them, the adsorption method is the easiest to operate and has significant advantages such as being economical and efficient, environment friendly, and not producing by-products (Mahmoodi et al., 2017; Almasian et al., 2015). Methods based on adsorption are effective for the simultaneous removal and recovery of PMG from wastewater. However, the adsorbent should be engineered appropriately for high efficiency, and easy separation for subsequent processes.

As a new class of crystalline porous materials, metal-organic frameworks (MOFs) with large surface area, adjustable pore size, and diverse structures are attractive in the environmental protection field (Zheng et al., 2018). Among them, MIL-101 is a porous metal-organic skeleton material formed by Cr^{3+} or Fe^{3+} and terephthalic acid coordination, with ultra-high specific surface area and pore volume (Ferey, 2005). The structure of MIL-101 (Fe) material is tunable, and various functionalities such as amino and sulfonic acid groups can be incorporated as needed for better adsorption performance (Feng and Xia, 2018). The MIL-101 or its variants are present in powder form with a large number of voids with few unsaturated metal centers (Abdi et al., 2017) which limit their use in water treatment industry due to difficulties envisage in particulate separation, reusability, and removing pollutants with a weak affinity for conventional MOF.

On the other hand materials such as biochar (BC), activated carbon (AC), clay and resin are used for adsorptive removal of PMG in water with low efficiency (Feng et al., 2020). Among these materials, BC readily available and can be synthesize by biogenesis solid substrate, show great economic promise (Liu et al., 2021), and due to it has a porous structure enriched with different functional groups. BC obtained from pyrolysis of waste biomass is widely used to remove pollutants from wastewater (Pan et al., 2021), but BC surface is negatively charged (Zhou et al., 2014) which rendered it as a poor adsorbent for PMG removal. On the other hand, due to its high mechanical strength and structural tunability BC is widely used as a carrier substrate.

Therefore, it is envisaged that a composite fabricated by loading appropriate MOF on BC carriers may overcome most of the difficulties encountered in the water industry in pollution control (Shang et al., 2022). The composites not only have the structural advantage of supporting MOF but also have enhanced specific surface area and composition stability in water, which can effectively solve the disadvantage of MIL-101 being too dispersed in water, while still maintaining high adsorption performance The selectivity of the composite for different pollutants can also be achieved using organic functional groups to modify surface acid-base properties (Wu et al., 2020). Previously MOF and modified BC are used to adsorb PMG in wastewater (Wei et al., 2018; Zhong et al., 2018) with limited success, particularly during substrate fabrication. To circumvent these limitations, we proposed in situ growth of MOF on BC.

Presently, we fabricated a new composite using BC as a substrate to impregnate MIL-101 MOF by solvothermal method and modified it with $-NH_2$ for adsorptive removal of PMG from water. First, the new substrate was extensively characterized by scanning electron microscopy, transmission electron microscopy, X-ray diffractometry, molecular spectroscopy, x-ray spectroscopy, and classical experimental measurements in batch mode. Then, a series of adsorption tests and fixed bed tests were conducted to explore the adsorption properties of the material, and DFT calculations were used to further investigate the influence of amino modification on the adsorption properties of PMG molecules on the surface of the material Finally, the efficacy of the new substrate for PMG removal was examined in a practical situation using industrial wastewater samples. The new adsorbents not only have excellent adsorption capacity for PMG, but also can solve the problem of agricultural solid waste disposal.

2. Materials and methods

2.1. Chemicals

All the chemicals received from the manufacturers were used without further purification. Deionized water (18.2 MΩ/cm) was used throughout the sample preparations. The details of the chemical reagents are listed in the Supplementary Material.

2.2. Preparation of adsorbents

BC for the preparation of adsorbent was obtained from a biomass pyrolysis power plant (China), was first washed with ultrapure water several times, oven-dried at 100 °C for 12 h, ground, and passed through a 100-mesh sieve to acquire the powder materials with small grains. The pristine BC was acquired by calcination at 500 °C at 5 °C/min heating rate under N_2 atmosphere for 4 h and then washed with HCl several times to remove magazines and heavy metals and dried for storage.

The NH_2-MIL-101@BC (NMBC) synthesis was carried out in three steps. In the first step, 0.12 g of BC was added to 80 ml N, N-dimethylformamide (DMF), sonicated and then stirred continuously for 0.5 h to obtain a homogeneous suspension. In the second step, aliquots of 0.002 M $FeCl_3 \cdot 6H_2O$ and 0.001 M 2-aminoterephthalic acid were dispersed into the suspension and stirred for 1 h to obtain a uniformity of the suspension. In the last step, the mixed suspension was poured into the PTFE-lined reaction kettle and placed in an oven at 120 °C for 24 h to grow the MOF structure. After cooling to room temperature and centrifuging for solid & solution separation, and the product was washed three times with DMF and ethanol respectively, and then oven-dried to obtain the final product. According to the mass ratios of MOF to BC, the adsorbents were named NH_2-MIL-101@BC (2:1) ($NMBC_{21}$), NH_2-MIL-101@BC (4:1) ($NMBC_{41}$), NH_2-MIL-101@BC (6:1) ($NMBC_{61}$), and NH_2-MIL-101@BC (8:1) ($NMBC_{81}$).

Meanwhile, MOF@BC composites without amino groups were prepared for comparison with those containing amino groups. The preparation process is similar to NMBC, except that the 2-aminoterephthalic acid was replaced with terephthalic acid (hereafter MIL-101@BC (2:1) (MBC_{21}).

The glass bead composite material was prepared by the thermal deposition method in order to reduce the loss of NMBC under high flow conditions (Fig. S10). 3 g treated glass beads with a diameter of 0.6–0.8 mm were put into a beaker, and a quantity of NMBC suspension was added. After mixing evenly, the glass beads were put into an oven at 100 °C for drying (in order to prevent bonding between glass beads, glass rods were used to stir at intervals). To increase the load thickness of NMBC on the surface of glass beads, NMBC suspension is added again when approaching the drying time. The total amount of NMBC suspension added is 2 ml, and 1 g of glass bead composite material containing 0.01 g NMBC was obtained.

2.3. *Characterization*

The morphology of adsorbents was observed using a scanning electron microscope (SEM, Hitachi SU8020). The transmission electron microscope coupled with energy dispersive spectroscopy was employed to explore the interior structure and elemental distribution of adsorbents (TEM-EDS, JEM-2100 F, Japan). The crystallographic structure of adsorbents was detected by the X-ray diffractometer (PANalytical, Netherlands). The ATR-FTIR spectra were obtained by an FT-IR spectrometer (Thermo Nicolet 6700, USA) in the 4000−500 cm^{-1} range to monitor changes in the functional groups on the sample surface. Raman spectrometer (HORIBA JOBIN YVON, LabRAM HR, Japan) was used to obtain Raman spectra. The chemical states of materials were acquired by X-ray photoelectron spectroscopy (XPS, Thermo ESCALAB250Xi, USA). The specific surface areas (SSAs) and pore size distribution were analyzed with the Brunauer-Emmett-Teller (BET) method (Autosorb-IQ3, Quantachrome, USA). Determination of zeta potential at different pH by zeta potential analyzer (Nano ZS90, USA) to determine the isoelectric point of the samples.

2.4. *PMG adsorption experiment*

Adsorption kinetics experiments were conducted in a conical flask, where PMG solution of 0.4 g L^{-1} and 50 ml was mixed with 0.02 g of adsorbent at a temperature of 298 K. The kinetic model utilized for this experiment can be found in Text S2. Meanwhile, adsorption isotherm experiments were carried out under varying temperature conditions of 298 K, 308 K, and 323 K, with 20 mg adsorbent added to 50 ml of different concentrations of PMG solution, all while subjected to spinning at 150 rpm. The adsorption isotherms and thermodynamic models were fitted utilizing the relevant equations in Text S2. To further investigate the adsorption performances of $NMBC_{61}$ on PMG, the same adsorption system was utilized, with the temperature maintained at 298 K, pH range between 2 and 10, and with the presence of different coexisting species. In addition, the regeneration and practical applications of the adsorbent were also probed. Finally, to evaluate the dynamic adsorption performance of $NMBC_{61}$, a fixed bed technique was utilized, and the concrete methods utilized can be found in Text S2.

2.5. *Computational methods*

Density functional theory (DFT) calculation has been applied to study the adsorption mechanism. Since the surface was mainly donated by ligand (Fan et al., 2022), the interactions between two ligands monomer and PMG were calculated by Gaussian16. Quantum chemical studies are performed using density functional theory (DFT) implemented in GAUSSIAN 16 package (Frisch et al., 2016). Geometry optimization and frequency analysis are calculated at B3LYP hybrid functional (Devlin et al., 1997) with GD3BJ dispersion correlation at 6-31G(d) basis sets. Electrostatic potential surfaces (ESP), Independent gradient model based on Hirshfeld partition (IGMH) (Johnson et al., 2010; Lu and Chen, 2022), and Charge density differences (CDD) between two fragments are performed to evaluate the interactions of structures. The analyses are performed by Multiwfn 3.8 (Lu and Chen, 2012) and VMD v 1.9.3 (Humphrey et al., 1996) molecular visualization software. For more information see Text S3.

3. Results and discussion

3.1. *Characterization of adsorbents*

A series of preliminary experiments were carried out to determine the best adsorbent for PMG adsorption and the optimal equilibration time (the details of the results are shown either in the main text or support documentation). Bare BC and composites of different proportions were also used as PMG adsorbents as controls. Our results show that $NMBC_{61}$ at 360 min show optimal PMG adsorption. Unless otherwise mention in subsequent experiments the $NMBC_{61}$ was used.

Fig. 1 shows the SEM and TEM micrographs of $NMBC_{61}$. The MOF grows on BC consistently preserving the octahedral structure of the MOF (Fig. 1(a-b)). The TEM images show that the MOF is well confined to grow on BC and element nitrogen, which can promote electron transfer, is widely distributed on the surface of the carbon matrix (Fig. 1(d)).

The XRD (Fig. 2(a)) was used to analyze the crystallinity and phase purity of $NMBC_{21}$, $NMBC_{41}$, $NMBC_{61}$, and MBC_{41}. The reference XRD spectrums of NH_2-MIL-101 and MIL along with BC and MOF are also shown in the diagram. The $NMBC_{x,1}$ nanocomposite retains the XRD peaks of BC in various proportions showing conformity of the crystal structures. The spectral signatures of the $NMBC_{x,1}$ are in good agreement with the reference data, and these composites have good crystalline growth and good crystallinity (Xie et al., 2017).

Fig. 2(b) shows the Fourier transformed infra-red spectra of the $NMBC_{x,1}$ nanocomposite resembles the spectra of benzene carboxylates. The untreated BC has strong absorption bands at 3418 cm^{-1} and 1086 cm^{-1}, corresponds to the –COOH derived H-bonding and C–O stretching vibrations, respectively (Weng et al., 2014; Fiorilli et al., 2017). In situ growth of MOF on BC resulted a significant change of the surface functional groups. The IR bands at 1576 cm^{-1}, 1393 cm^{-1}, and 768 cm^{-1} correspond to –C=O, aromatic C=C, and Fe–OH vibrations (Xie et al., 2017), (Liu et al., 2019). In NMBC, the IR band at 1256 cm^{-1} corresponds to -C-N stretching vibrations of 2-aminoterephthalic acid. The loading of the amino group splits the hydroxyl band at 3438 cm^{-1} into two moderately intense bands (Yantasee et al., 2004), while the absorption band of MBC at this point does not change significantly, which shows that the NMBC is successfully loaded with NH_2-group on its surface. The nanocomposites resulted by in situ growth of MOF material on BC contains large proportions of oxygen-containing functional groups and iron oxides, which provide efficient electron transfer mediators and complexation ligands for the complexation of PMG on nanocomposite (Fig. 2(b)).

From the Raman spectral data show more defects intensity in nanocomposites compared to untreated BC, the $NMBC_{61}$ has the largest peak intensity ratio (Fig. 2(c)), so it can provide the highest adsorption sites (Zhang et al., 2016). Variation of zeta potential of $NMBC_{61}$ with pH (Fig. 2(d)) shows that the isoelectric point is about ~8.00 and the surface is positively charged between pH 2.00 and 8.00.

The nitrogen gas adsorption of BC and the synthesized composites (Fig. 2(e)) show type IV isotherms implying that the materials are mesoporous. Capillary coalescence occurs in the BC, $NMBC_{21}$, and MBC_{21}, and the closed rings generated by the isotherms form H4

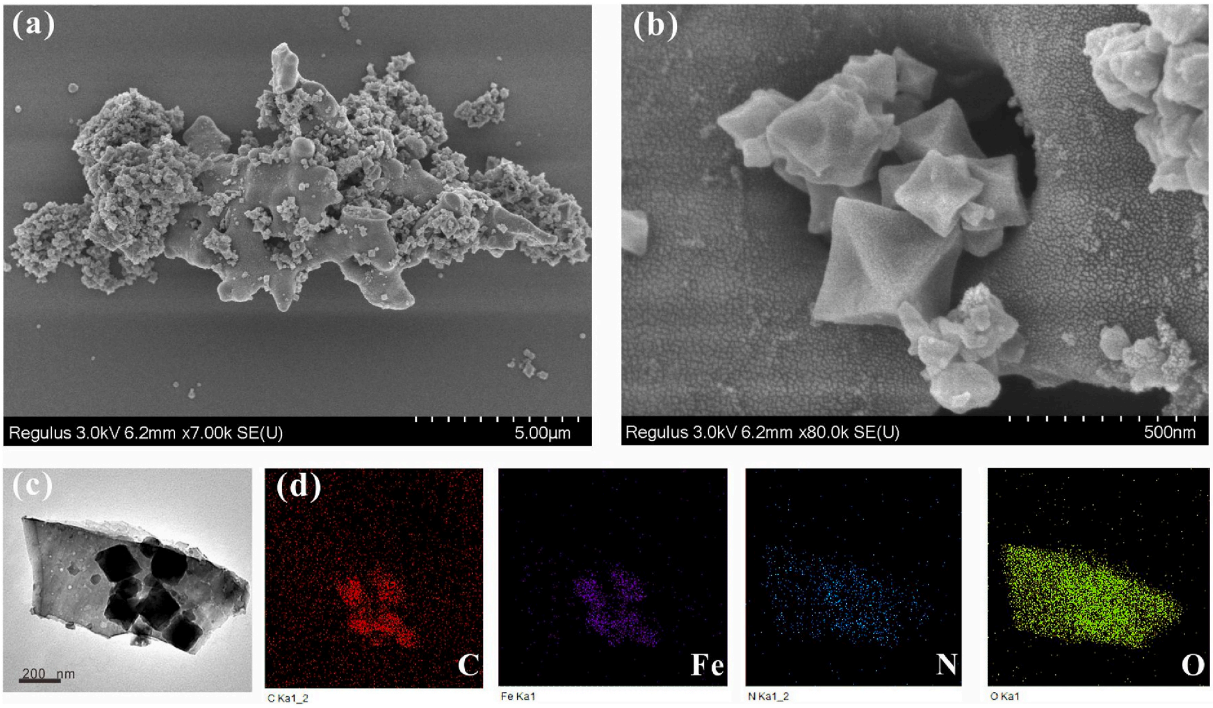

Fig. 1. (a–b) SEM images; (c) TEM image; (d) element mapping of $NMBC_{61}$.

hysteresis rings, which indicates that the material has a narrow slit-like shape. In $NMBC_{61}$ nitrogen gas adsorption increases gently in the low-pressure section, and at a relative pressure P/P_0 of about 0.9, the H1-type hysteresis ring formed has a sudden increase indicating that the material has a large pore size distribution, uniformity and pore channel connectivity, which are conducive to the adsorption. Fig. 2(f) shows that pore sizes of the composites are in the range of 2–3 nm. According to the International Union of Pure and Applied Chemistry (IUPAC) to classify the characteristics of pores of porous materials, the pore sizes are determined by their diameters: microporous (<2 nm), mesoporous (2–50 nm), and macroporous (>50 nm), and all our composites belong to mesoporous. In addition, the volumetric mean particle size of NMBC (99.373 μm) is significantly larger than that of NH_2-MIL-101 (18.833 μm) was found by laser particle size analyzer, indicating the composite solves the disadvantage of MOF being too dispersed in water and can be better recycled. As in Table S1, both the specific surface area and pore size of $NMBC_{61}$ is enhanced significantly compared to BC, $NMBC_{21}$ or MBC_{21}. And it is worth noting that although the specific surface area of $NMBC_{21}$ is slightly smaller than that of MBC_{21}, the adsorption capacity is significantly increased (Fig. 3(a)), indicating that the introduction of amino functional groups on the ligand can effectively increase the adsorption sites on the material surface.

3.2. Effect of reaction time on PMG adsorption

Fig. 3(a) shows the variation of PMG adsorption on bare BC and other nanocomposites as a function of reaction time at pH 6.0. In all cases an apparent saturation of PMG adsorption is reached within 360 min, the PMG adsorption can be divided into three domains, fast, slow and equilibrium stages (Zhao et al., 2014). The PMG adsorption by the bare biomass charcoal is the lowest which is accompanied by desorption phenomenon. When the MOF is amino functionalized, the PMG adsorption increases as a function of $\left(\frac{amino-MOF}{BC}\right)$ reaching an optimal adsorption in $NMBC_{61}$ (Fig. 3, $\left(\frac{amino-MOF}{BC}\right) = \frac{6}{1}$). The amino modification of the composite renders net positive surface charge thus favoring PMG adsorption (Liu et al., 2019). The maximum PMG adsorption of 137.4 mg L^{-1} when the $\left(\frac{amino-MOF}{BC}\right)$ ratio reaches beyond 6:1. However, the overgrowth of MOF on BC surface and blocking pores by agglomeration has reduced PMG adsorption on $NMBC_{81}$ significantly (Fig. 3(a)). Table S2 shows a comparison of the optimal PMG adsorption capacity of our nanocomposites with the other materials reported elsewhere. The $NMBC_{61}$ nanocomposite shows the highest PMG adsorption using 0.4 g L^{-1} adsorbent at 323 K in pH 6.00 solution.

The chemical kinetics of PMG adsorption on $NMBC_{21}$, $NMBC_{41}$, $NMBC_{61}$, and $NMBC_{81}$ was also examined using Lagrange quasi primary, quasi secondary and intraparticle diffusion and liquid film diffusion adsorption kinetic models and the data are shown in Tables S3, S4, S5 and Fig. S1. In agreement with previous results (Lalley et al., 2016) the PMG adsorption on BC derived composites follow quasi-second order kinetics according to data fitting (Fig. S2(b), $R^2 > 0.98$). According to Weber-Morris intraparticle diffusion model (Fig. S2(c)), the PMG adsorption can ascribed by three stages; surface adsorption, intraparticle diffusion, and steady state adsorption (Zhao et al., 2014), and the adsorption rates decrease gradually ($K_{P3} < K_{P2} < K_{P1}$). The steep part of Fig. S2(c) is limited by the external membrane diffusion, and PMG is adsorbed on the surface through the solid-liquid boundary layer until the outer surface is saturated, and the linear intercept indicates the influence of external mass transfer, generally the larger the intercept the greater the degree of influence. Due to the increase in mass transfer resistance, the pore diffusion seems controlling overall PMG adsorption rate. Finally the equilibrium phase is limited by the microporous diffusion where the adsorption sites reach saturation and the adsorption rate reaches a minimum (Zhao et al., 2014). The linear fit did not cross the origin, indicating that internal diffusion is not the main reason for the rate determination (Rajabi et al., 2016). In addition, as shown in Fig. S2 (d), the fit of the liquid film diffusion model is smaller than that of the intraparticle diffusion model, showing that the liquid film diffusion mechanism is also not the main mode of the adsorption process.

3.3. Effect of solution pH on adsorption

pH, as one of the most significant parameters in the adsorption process, could affect and change both adsorbent and adsorbate surface charge and manipulate the pollutant removal ability of the adsorbent.

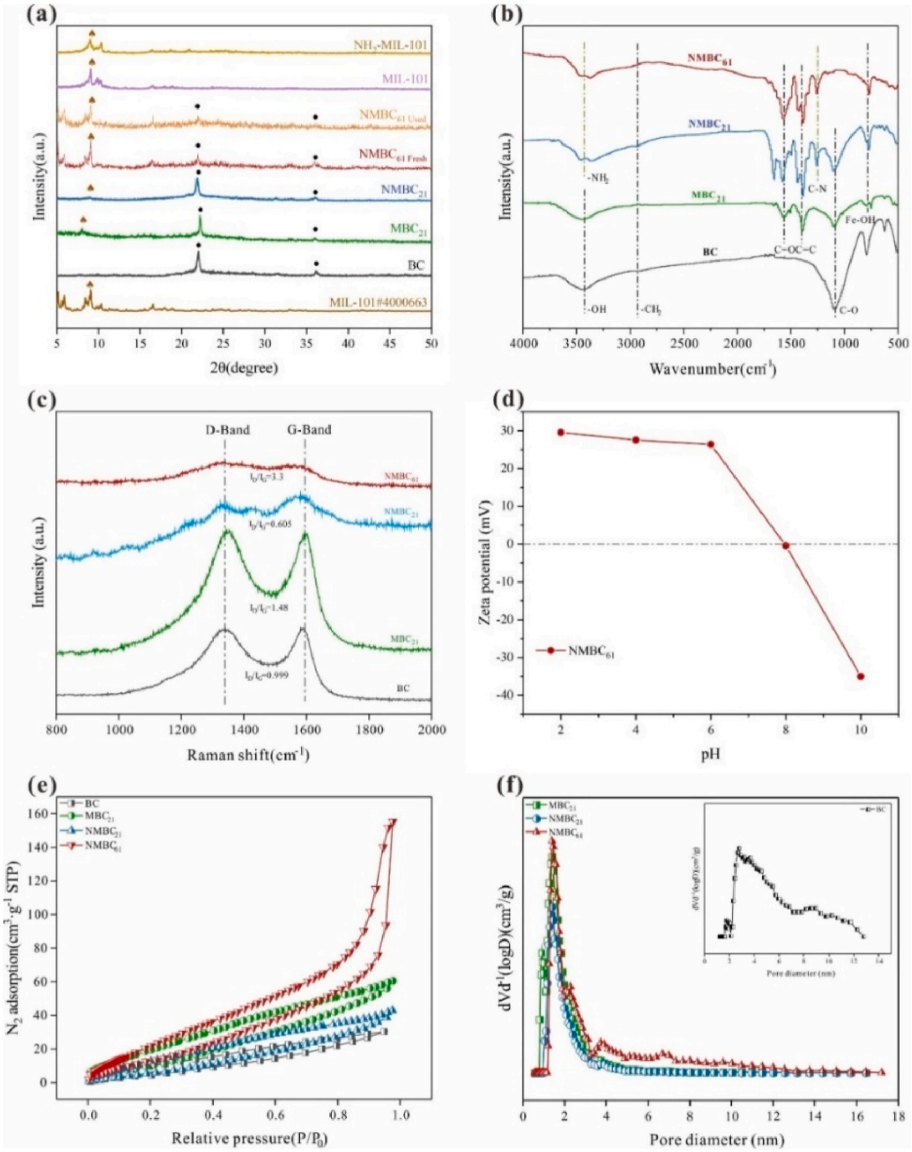

Fig. 2. (a) XRD patterns, (b) FTIR spectra, (c) Raman spectra, (d) Zeta potential of $NMBC_{61}$ with different pH (e) Nitrogen adsorption isotherms, (f) pore size distribution of adsorbents.

Therefore, finding the proper pH value for the adsorption experiment becomes very important (Mahmoodi et al., 2019). The effect of solution pH on the PMG adsorption by $NMBC_{61}$ is shown in Fig. 3(c). The PMG speciation diagram as a function of pH is also shown in Fig. 3(d). PMG shows a weak tri-protonic acid character. When pH > 2.20, the anionic PMG species dominate in solution. Variation of zeta potential of $NMBC_{61}$ suspension as a function of pH is shown in Fig. 2(d). When pH varies between 2.00 and 8.00, the particulate surface is positively charged favoring PMG adsorption. When pH $= 2$, the neutral PMG species which dominates in solution show weak affinity towards $NMBC_{61}$ sites. When solution pH is between 4.00 and 6.00, the $NMBC_{61}$ surface is positively charge showing optimal affinity for PMG adsorption. When pH > 8.00 the anionic forms of PMG dominate and the $NMBC_{61}$ surface sites negatively charge. Under this situation the PMG adsorption on $NMBC_{61}$ diminishes as shown in Fig. 3(c). Therefore, the positive and negative charges on the surface of the $NMBC_{61}$ have a significant effect on the adsorption capacity of PMG. In conclusion, the electrostatic effect plays an important role in the adsorption process.

3.4. PMG adsorption isotherms and thermodynamic parameters

Fig. 3(b) shows the isotherms of PMG adsorption on $NMBC_{61}$ as a function of temperature (298 K, 308 K and 323 K). In all temperatures examined the PMG adsorption by $NMBC_{61}$ can be best interpreted in terms of the Langmuir model ($R^2 > 0.995$; Table S6, Langmuir data). The optimal PMG adsorption by $NMBC_{61}$ increases with the system temperature showing an endothermic process (Fig. 3(b)). Within the Langmuir domain (Wang et al., 2015), PMG adsorption can be further divided into four sub-domains; a. Preferential adsorption ($0< R_L <1$), b. Linear adsorption ($R_L = 1$), c. Non-preferential adsorption ($R_L >1$), and d. Irreversible adsorption ($R_L = 0$) (Mahmoodi et al., 2017) based on the separation factor calculated according to equation (S8). Values calculated at 298 K, 308 K and 323 K were 0.707, 0.506 and 0.138, respectively, ranging between 0 and 1. Accordingly the PMG adsorption on $NMBC_{61}$ has fallen into the preferential adsorption category, irrespective of the system temperature (Iqbal and Ashiq, 2007).

The thermodynamic parameters of PMG adsorption by $NMBC_{61}$ were calculated using equation (S11) and $\Delta G = \Delta H - T\Delta S$ relationship as shown in Fig. S2. In thermodynamics parameter estimations, we used

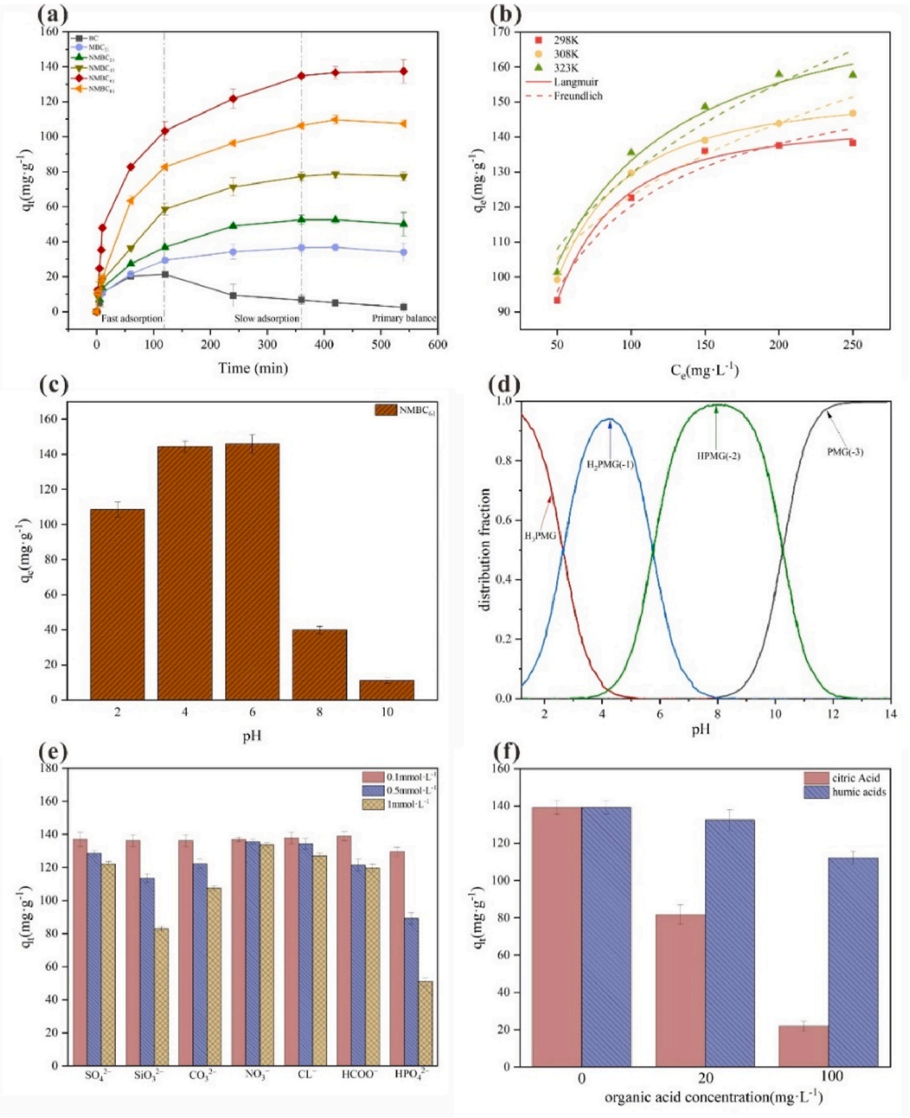

Fig. 3. (a) Effect of contact time, (b) PMG adsorption isotherm (c) Effect of initial pH on PMG adsorption performance, (d) The speciation of PMG, (e) Effect of competitive anions, (f) Effect of dissolved organic matter on PMG adsorption.

the initial conditions as in Langmuir isotherm formulations. The Langmuir model assumed energetically homogeneous surface sites. The electrostatic charging component between PMG and NMBC$_{61}$ surface sites was neglected in deriving necessary mass action coefficients (e.g., Langmuir coefficient). Further, the adsorption isotherms were constructed at a given pH (~6.00 presently) which implies that the fraction of PMG and surface sites remained constant. Therefore, we can assume that the activities of both surface and solute species are directly proportional to their concentrations. Under these constraints, we assumed that the resulting thermodynamic parameters reported in this work are conditional to the experimental parameters used. Our data show that the free energy of PMG adsorption is non-spontaneous and increases with the system temperature, and the relevant thermodynamic parameters are shown in Table S7. The positive value of the free energy ΔG^{θ} indicates that the adsorption process is non-spontaneous, indicating that it is driven by weak van der Waals forces and is an active adsorption process, and increasing the temperature favors the adsorption by reducing activity energy values. The enthalpy change ΔH^{θ} is positive, showing an endothermic process, which seems consistent with the data shown in Table S6 and experimental results. Increasing the reaction temperature within a certain range is beneficial to the adsorption process, and the calculated value of ΔH^{θ} is 165.735 kJ mol^{-1} exceeded the critical enthalpy value of physical adsorption (40 kJ mol^{-1}), indicating that chemical bond force is the main force for the adsorption of PMG, and hydrogen bond force and van der Waals force may exist. The entropy ΔS^{θ} is positive, indicating that the adsorption of PMG on the material is an entropy-increasing process. (Wang et al., 2018).

The linear fit of the Arrhenius equation is shown in Fig. S4. The activation energy is an important factor in determining the reaction rate. At room temperature, the reaction rate is fast for the activation energy less than 40 kJ mol^{-1}; the reaction rate is slow for the activation energy greater than 120 kJ mol^{-1} (Zhao et al., 2021). From the kinetic analysis this adsorption process is consistent with the quasi-second-order kinetic model, so the apparent activation energy was calculated using the reaction rate k_2 of the quasi-second-order kinetic model. The apparent activation energy of quasi-second-order reaction kinetics of PMG in this ion exchange process is 38.87 kJ mol^{-1}, and the apparent rate constant k_2 becomes larger as the temperature of the exchange reaction system of PMG and adsorbent increases, indicating that the higher the temperature, the exchange reaction dominates (Campbell and Sellers, 2013), which is consistent with our data. Also E_a <40 kJ mol^{-1} indicates that this adsorption process proceeds rapidly. Although the fits of PMG

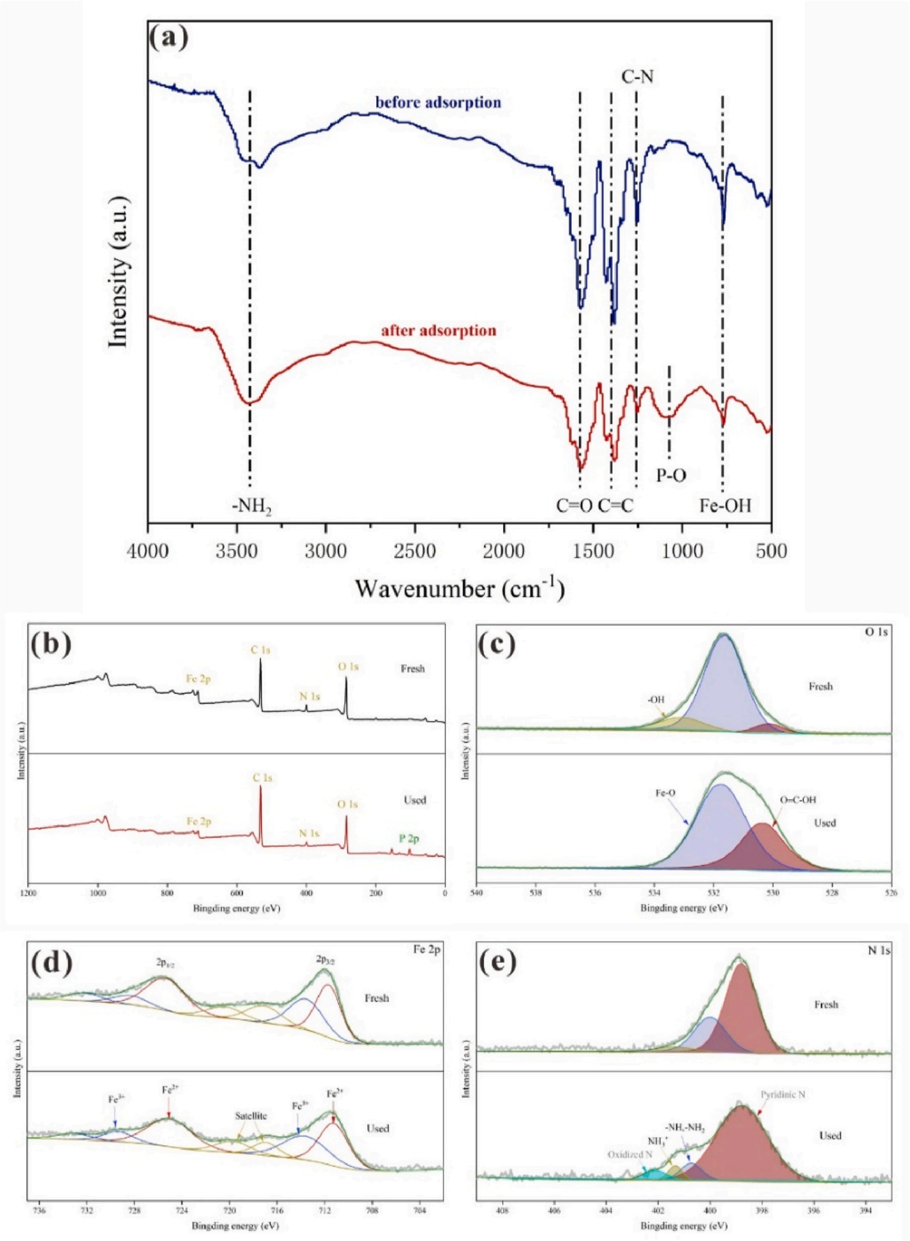

Fig. 4. (a) FTIR spectrums, (b) XPS full spectrum, (c) O 1s XPS, (d) Fe 2p XPS, (e) N 1s XPS of $NMBC_{61}$ before and after PMG adsorption.

adsorption into Freundlich isotherm is not perfect, still the n parameter of the model lies between 2 and 10 (Table S3) implying rapid process (Li et al., 2018).

3.5. *Matrix effects on PMG adsorption*

Wastewater often contains large proportions of inorganic and organic species that may inhibit or enhance PMG adsorption on $NMBC_{61}$. To determine the competing effect between anions and organic compounds common in wastewater on PMG adsorption, SO_4^{2-}, SiO_3^{2-}, CO_3^{2-}, NO_3^-, Cl^-, $HCOO^-$, HPO_4^{2-}, citric acid and humic acid were introduced to the reactor discretely, at three concentrations, viz., anions 0.1, 0.5 and 1 mM, humic acid and citric acids 20 and 100 mg. L^{-1}. The 1 mM HPO_4^{2-} shows highest competition with the PMG for adsorption sites (Ballinger et al., 2015; Dong et al., 2017) (Fig. 6(a)). The competing effect of SiO_3^{2-} and CO_3^{2-} for PMG adsorption is also marked whereas the SO_4^{2-} shows an intermediate behavior. However, the effect of NO_3^-, Cl^-, and $HCOO^-$ for PMG adsorption is not significant (Fig. 3(e)). These observations show different binding behavior between PMG and the competing anions for surface sites. PMG present as H_2PMG^- and $HPMG^{2-}$ around pH 6.00 (Fig. 3(d)). When pH > 2, PMG forms H_2PMG^- and $HPMG^{2-}$ in solution, therefore SO_4^{2-} hinders PMG adsorption by a competition. Being inert ions NO_3^-, and Cl^- form outer sphere surface complexes with $NMBC_{61}$ sites (Xie et al., 2014), (Wang et al., 2016); hence they do not compete significantly with PMG which forms specific surface bonding via inner sphere complexing (Saadat et al., 2018). In contrast, both SiO_3^{2-} and CO_3^{2-} tend to increase solution pH disturbing chemical speciation thus reducing PMG adsorption (Ballinger et al., 2015; Dong et al., 2017). As shown in Fig. 3(f), the effect of humic acid and citric acid on PMG adsorption by $NMBC_{61}$ deserves a discussion.

Humic acids are defined operational to account for a large array of base soluble organic compounds whereas citric acids represent a well-defined small molecule in the nature. As shown in Fig. 3(f), humic acid did not have a great effect on the PMG adsorption, while the small-molecule citric acid has a marked negative impact on the PMG adsorption (PMG adsorption capacity decreased by 82% at 100 mg L^{-1} citric

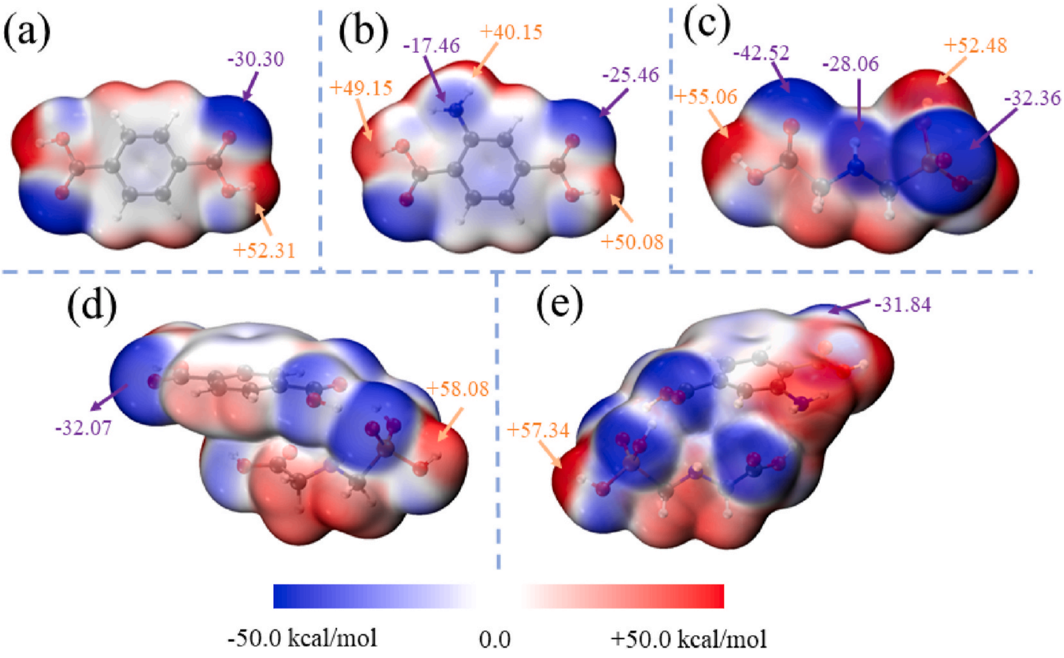

Fig. 5. ESP of (a) BDC, (b) BDC-NH_2, (c) PMG, (d) a3, (e) b3.

acid dosing). Both citric acid and PMG are small molecules with comparable size. Therefore, they do compete for surface sites effectively. Being a cross-link polymeric mixture, humic acid seems not covering same sites used for PMG or citric acid adsorption. Therefore, the humic acid shows indifferent behavior towards PMG adsorption on $NMBC_{61}$. When compared to experimental settings, the concentrations of both humic and citric acids are very low in natural water, therefore they play a minor role when treating PMG laden wastewaters (Möller and Sylvester 2008).

3.6. Adsorption mechanism

3.6.1. Adsorption characteristics according to experiments

The functional groups on the adsorbent surface before and after the reaction were analyzed using Fourier infrared spectroscopy to further investigate the mechanism of action during the adsorption of PMG by $NMBC_{61}$, and the analysis is shown in Fig. 4(a).

The vibration at 768 cm^{-1} can be attributed to the fact that Fe–OH exhibits a large number of active sites after the resolution of water adsorption, and after the adsorption of PMG, the vibration occurs here indicating Fe–OH weakening (Liu et al., 2019), instead a broader and stronger peak appears at 1052 cm^{-1}, corresponding to the vibration of the v3 band of $H_2PO_4^2$ or HPO_4^- (Persson et al., 1996), a phenomenon is consistent with the ionic morphology of the phosphate group in PMG at this pH condition, it shows that the adsorption process involves the complexation of functional groups. The characteristic peak of the adsorbent is significantly weaker after adsorption at 1255 cm^{-1}, which is due to the involvement of the –NH_2 of the adsorbent in the adsorption reaction and hydrogen bonds are formed with the groups on the pollutant molecules, enhancing the adsorption effect. The above analysis shows that the hydroxyl and amino groups of the adsorbent are the main locations of phosphate group substitution in PMG during the adsorption process. The XPS analysis of the PMG- $NMBC_{61}$ composite further supports IR spectral data.

As shown in Fig. 4(b) the peak at 128.7 eV is due to P2p binding energy upon PMG adsorption. The peaks at 530.1 eV and 531.8 eV are attributed to oxygen present in amino terephthalate and Fe–OH in MOF, while the binding energy peak at 533.1 eV corresponds to surface OH groups on the composite which diminished upon PMG adsorption. The P2p XPS signals correspond to phosphate in PMG exchanged with OH sites (Fig. 4(c)), and the proportion of the O═C–OH group increased obviously, indicating that the adsorbent formed a complex with -PO$(OH)_2$. The Fe2p spectrum (Fig. 5(d)) convolved into two components at 711.5 eV and 714.2 eV, attributed to Fe(II) and Fe(III), respectively, and after PMG adsorption, the characteristic Fe (III) peak broadens and Fe (II) → Fe (III) partially forming Fe oxides on the composite (Borggaard and Gimsing, 2008). Iron hydrous oxide has a high affinity for PMG showing enhanced adsorption. However, in general, the ratio of the two forms of Fe changed little before and after adsorption, indicating that the properties of adsorbed materials are stable. The N1s of $NMBC_{61}$ deconvolved into three peaks corresponding to pyridine N, –NH_2 and NH^{3+}. Upon PMG adsorption on $NMBC_{61}$ the deconvolved spectrum shows four peaks due to oxidized N in adsorbed PMG proving the importance of amino groups. In the N1s profile ((Fig. 5(e)), after adsorption, the two peaks of N ls moved towards high binding energy, indicating that the chemical environment of protonated amino groups on the adsorbent changed, and it speculated that amino groups provided a large number of active sites for the materials. At the same time, the obvious reduction of the –NH_2 peak area also proves that the amino group on the material is the main substitution site of PMG. In addition, intermolecular weak interaction also played a role in the whole adsorption process, so it is necessary to further explore.

3.6.2. Molecule interaction mechanism according to DFT calculation

According to the above analysis, further studies should be conducted on the weak interaction between PMG and ligands. The bimolecular conformations of the ligand and PMG are shown in Fig. S4, and conformations with the lowest energy (a3, b3) were selected for the analysis. Fig. 5 displays the electrostatic potential (ESP), which is used to predict the adsorption sites between PMG and ligands. Relevant parameters, such as the molecular polarity index (MPI), were calculated and listed in Table S8. The IRI isosurface map and RDG scatter plots were utilized to determine the type and relative strength of interactions. In addition, through the calculation and analysis of differential charge density (CDD), the spatial distribution information of charge movement and bonding polarization direction in the coupling process of bonding and bonding electrons can be obtained clearly. Through analyzing the ESP distribution, IRI isosurface map, RDG scatter plots, and CDD, the

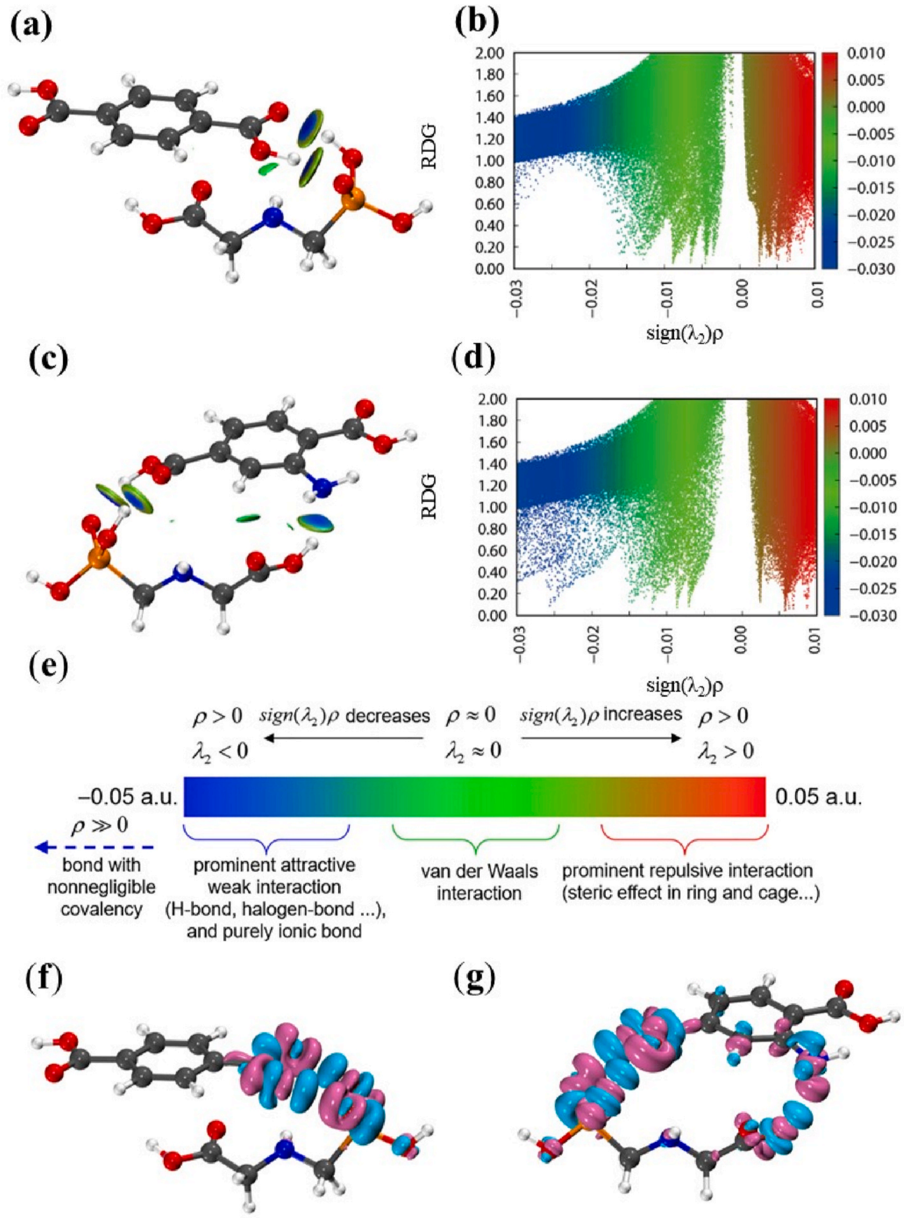

Fig. 6. (a) The IRI isosurfaces of a3, (b) RDG scatter plot of a3, (c) IRI isosurfaces of b3, (d)RDG scatter plot of b3, (e)Standard coloring method and chemical explanation of sign (λ2)ρ on isosurfaces, (f) The CDD of a3, (g) The CDD of b3.

differences in the adsorption mechanism of PMG on MOFs with or without functionalization can be reasonably explained.

ESP can be utilized to predict and explain the relative orientation of molecules in complex conformations. In Fig. 5(b), after introducing $–NH_2$, the positive polar region of ligand increased (Table S9), indicating that $–NH_2$ is more likely to act as additional adsorption sites and attract the negative ESP region of PMG, forming a more stable structure.

The IRI isosurface and RDG scatter plot of compounds formed between PMG and BDC, BDC-NH2 are shown in Fig. 6. Standard coloring method and chemical explanation of sign (λ2)ρ on IRI isosurfaces (Lu and Chen, 2022) were shown in Fig. 6(e). The green isosurface exists through all the conformations, which indicated that van der Waals (vdW) interactions always existed, whether functionalized or not. In addition, scattering in regions near −0.014a.u. And RDG <0.5 indicates weak hydrogen bonding. In Fig. 6(c) and (d), IRI can well reveal the regions corresponding to each chemical bond, and it can be seen that hydrogen bonds are formed between molecules, among which O–H bonds form isoplanes in the direction of $–NH_2$. Compared with BDC, there are more green isoplanes, indicating that $–NH_2$ provides additional vdW forces. The mechanism of the interaction between the two ligands and PMG molecules can be further analyzed by the results of charge density, with blue regions representing charge accumulation and purple regions representing charge reduction. Fig. 6 (f) shows that in the adsorption process of PMG by BDC, charge accumulation mainly occurs on -P═O in phosphate groups and -*O*-H in carboxyl groups of BDC, and charge loss mainly occurs on O atoms in carboxyl groups of BDC, indicating that electron transfer occurs between them, and non-covalent interaction is formed between them. From Fig. 6 (g), it can be seen that in PMG, charge reduction occurs on -P═O in the phosphate group, charge loss occurs around the O atom in $BDC-NH_2$ carboxyl group and N atom in the amino group, and electron aggregation occurs around H atom on the group. According to the above analysis, The modification of amino groups resulted in more charge transfer between the ligand and PMG molecules. In summary, the functionalized ligand can form new configurations of the PMG towards functional groups, which can provide additional interaction isosurfaces, so the utilization of $–NH_2$ ligand functionalization can be applied to achieve efficient removal of PMG.

3.7. *Regeneration of adsorbent*

A separate set of adsorbent regeneration experiments were conducted to examine its practicality in applying NMBC$_{61}$ for PMG control. Regeneration of the NMBC$_{61}$ were carried out with 1 M NaOH at 80% PMG desorption efficiency. As in Fig. S7(a), the PMG adsorption capacity declined from 158 to 121 mg g^{-1} after three cycles. Although the PMG adsorption reduced the regenerated NMBC$_{61}$ can still be used several cycles before deactivation. In agreement with the data presented so far, some fractions of PMG seem to bind to NMBC$_{61}$ irreversibly, therefore the efficacy of the material degrade after excessive repeated use. It is worth noting that the used NMBC$_{61}$ showed the same crystal shape as that before adsorption, which proved that the composite has good stability. Meanwhile, the leached of iron during four reactions of the adsorbent was explored, as shown in Fig. S7(b). After three cycles, the leached amount of iron in the reaction solution gradually decreased from 1.543 mg L^{-1} to 0.983 mg L^{-1}, indicating a relatively low decrease in the leaching rate of iron. Overall, the NMBC$_{61}$ composites have good regeneration performance and reuse value.

3.8. *Practical application of adsorbent*

The application of NMBC$_{61}$ as an adsorbent in the removal of PMG in wastewater is shown in Fig. S8. Although the matrix of the wastewater is complex, the NMBC$_{61}$ possesses good capacity to remove 85% of PMG.

3.9. *Fixed bed column adsorption removal of PMG*

In order to evaluate the dynamic PMG adsorption performance of NMBC$_{61}$, continuous transport was used to adsorb PMG in water, and the schematic diagram of the device is shown in Fig. S9. Fig. 7 shows the PMG penetration curves at different affecting factors.

Dynamic adsorption results of PMG under different conditions as shown in Table S10, and according to the dynamic adsorption test, the optimum conditions were as follows: packing height was 1 cm, influent flow rate was 0.7 ml min^{-1}, reaction pH was 6, and initial concentration of PMG solution was 100 mg L^{-1}. Under these conditions, the maximum unit adsorption capacity of PMG on a fixed bed column was 161.3 mg g^{-1}. In this study, three adsorption models, Thomas, Yoon-Nelson and Yan, were selected to carry out fitting analysis on the dynamic adsorption process of PMG water by NMBC-glass beads and model parameters under different operating conditions as shown in Table s11. According to the model fitting diagram (Tables S11 and S12), it can be seen that Yan model can better describe the breakthrough curve in the fixed bed column, and detailed conclusions are found in Text S5. The rate constants calculated from the model fit provide theoretical guidance for the design and optimization of the fixed bed adsorption process.

4. Conclusions

We fabricated NMBC$_{61}$ using rice husk derived BC by a solvothermal method as an efficient composite for PMG adsorptive remediation of wastewater. At pH 6.00 typical of natural waters, the maximum PMG adsorption capacity of NMBC$_{61}$ is 186.71 mg. g^{-1} when 0.4 g. L^{-1} adsorbent is used. The PMG adsorption process is modeled by pseudo-second order kinetics and Langmuir models. The PMG adsorption on NMBC$_{61}$ is endothermic. NMBC$_{61}$ can adsorb PMG through electrostatic interaction and ligand complexation, and the hydroxyl and amino groups on NMBC$_{61}$ are active for PMG adsorption by anion exchange processes. DFT calculations demonstrated that adsorption involves weak interactions, such as vdW and weak hydrogen bond, and its type and strength are affected by the substitution functional groups. The common solutes found in wastewater do not interfere significantly with PMG adsorption. NMBC$_{61}$ has an optimal adsorption capacity between pH 2 and 6 and it maintain over 85% efficiency in multiple cycles. The dynamic adsorption capacity of NMBC$_{61}$was also investigated. These unique characteristics of NMBC$_{61}$ show a potential in treating organic pollutants in natural and wastewaters.

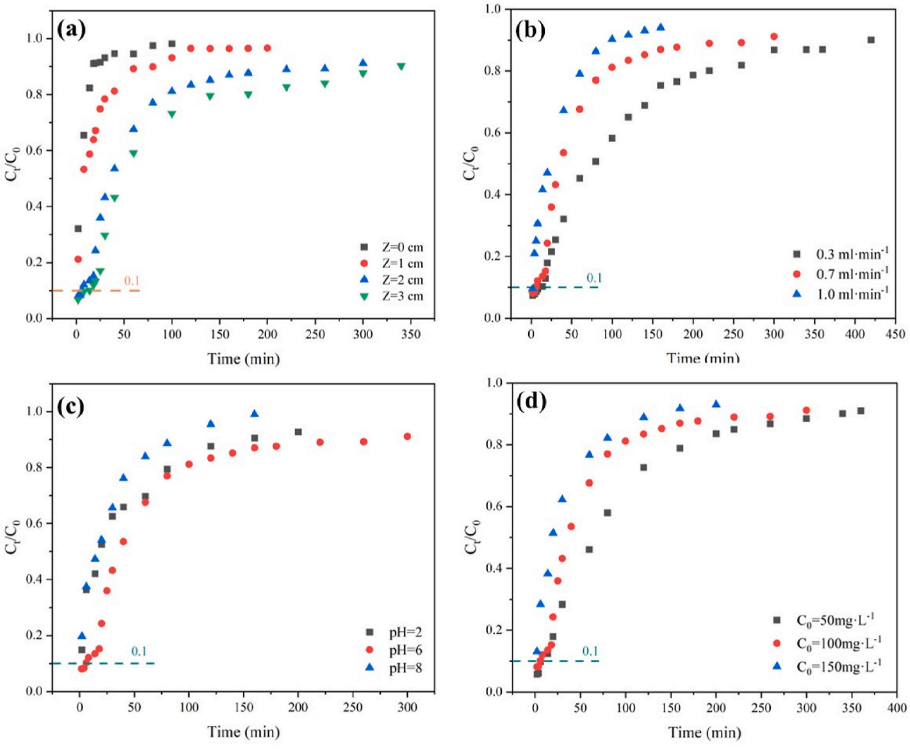

Fig. 7. Effect of (a) column height, (b) flow rate, (c) initial pH, (d) PMG concentration on adsorption of PMG breakthrough curve.

Credit author statement

Qi Wang: Investigation, Methodology, Formal analysis, Data curation, Writing - original draft. **Kang-Ping Cui:** Supervision, Conceptualization, Funding acquisition. **Tong Liu:** Investigation, Writing - review & editing. **Chen-Xuan Li:** Writing - review & editing. **Jun Liu:** Writing - review & editing. **Dian-Chao Kong:** Writing - review & editing. **Rohan Weerasooriya:** Writing - review & editing. **Xing Chen:** Supervision, Conceptualization, Funding acquisition.

Declaration of competing interest

The authors declare that they have no known competing financial interests or personal relationships that could have appeared to influence the work reported in this paper.

Data availability

No data was used for the research described in the article.

Acknowledgements

The work was supported by National Key R&D Program of China (2019YFC0408500), Major science and technology projects of Anhui Province (202003a07020004), Hefei key common technology R&D project (2021GJ067, 2021GJ069).

Appendix A. Supplementary data

Supplementary data to this article can be found online at https://doi.org/10.1016/j.chemosphere.2023.138827.

References

Abdi, Jafar, Vossoughi, Manouchehr, , Niyaz Mohammad Mahmoodi, Alemzadeh, Iran, 2017. ’Synthesis of metal-organic framework hybrid nanocomposites based on GO and CNT with high adsorption capacity for dye removal. Chem. Eng. J. 326, 1145–1158.

Almasian, Arash, Niyaz Mohammad Mahmoodi, Ebrahim Olya, Mohammad, 2015. ’Tectomer grafted nanofiber: synthesis, characterization and dye removal ability from multicomponent system. J. Ind. Eng. Chem. 32, 85–98.

Ballinger, B., Motuzas, J., Miller, C.R., Smart, S., da Costa, J.C.D., 2015. Nanoscale assembly of lanthanum silica with dense and porous interfacial structures. Sci. Rep. 5.

Borba, Lana Lima, Cuba, Renata Medici Frayne, Teran, Francisco Javier Cuba, Castro, Martha Nascimento, Mendes, Thiago Augusto, 2019. Use of Adsorbent Biochar from Pequi (Caryocar Brasiliense) Husks for the Removal of Commercial Formulation of Glyphosate from Aqueous Media. Braz. Arch. Biol. Technol. 62.

Borggaard, O.K., Gimsing, A.L., 2008. ’Fate of glyphosate in soil and the possibility of leaching to ground and surface waters: a review. Pest Manag. Sci. 64, 441–456.

Campbell, C.T., Sellers, J.R.V., 2013. ’The entropies of adsorbed molecules (vol 134, pg 18109, 2012). J. Am. Chem. Soc. 135, 13998, 98.

Chen, Yong, Wu, Feng, Lin, Yixin, Deng, Nansheng, Bazhin, Nikolai, Glebov, Evgeni, 2007. ’Photodegradation of glyphosate in the ferrioxalate system. J. Hazard Mater. 148, 360–365.

Devlin, F.J., Stephens, P.J., Cheeseman, J.R., Frisch, M.J., 1997. ’Ab initio prediction of vibrational absorption and circular dichroism spectra of chiral natural products using density functional theory: camphor and fenchone. J. Phys. Chem. A 101, 6322–6333.

Dong, S.X., Wang, Y.L., Zhao, Y.W., Zhou, X.H., Zheng, H.L., 2017. ’La3+/La(OH)(3) loaded magnetic cationic hydrogel composites for phosphate removal: effect of lanthanum species and mechanistic study. Water Res. 126, 433–441.

Fan, Sheng, Lu, Xinru, Li, Haoliang, Du, Xiaodong, Huang, Xiaoyu, Yao, Ma, Wang, Juan, Tao, Xueqin, Dang, Zhi, Lu, Guining, 2022. ’Efficient removal of organophosphate esters by ligand functionalized MIL-101 (Fe): modulated adsorption and DFT calculations. Chemosphere 302.

Feng, Dan, Xia, Yan, 2018. ’Comparisons of glyphosate adsorption properties of different functional Cr-based metal-organic frameworks. J. Separ. Sci. 41, 732–739.

Feng, Dan, Audrey Soric, Olivier, Boutin, 2020. ’Treatment Technologies and Degradation Pathways of Glyphosate: A Critical Review. Science of the Total Environment, p. 742.

Ferey, G., 2005. ’A chromium terephthalate-based solid with unusually large pore volumes and surface area, 309, pg 2040 Science 310 (2005), 1119, 19.

Fiorilli, S., Rivoira, L., Cali, G., Appendini, M., Bruzzoniti, M.C., Coisson, M., Onida, B., 2017. ’Iron oxide inside SBA-15 modified with amino groups as reusable adsorbent for highly efficient removal of glyphosate from water. Appl. Surf. Sci. 411, 457–465.

Frisch, M.J., Trucks, G.W., Schlegel, H.B., Ge, Scuseria, Man Robb, Cheeseman, J.R., Scalmani, G., Barone, V.P.G.A., Petersson, G.A., Nakatsuji, H.J.R.A., 2016. Gaussian 16, Revision A. 03, vol. 3. Gaussian’, *Inc.*, Wallingford CT.

Hu, Y.S., Zhao, Y.Q., Sorohan, B., 2011. Removal of glyphosate from aqueous environment by adsorption using water industrial residual. Desalination 271, 150–156.

Humphrey, William, Dalke, Andrew, Schulten, Klaus, 1996. ’VMD: visual molecular dynamics. J. Mol. Graph. 14, 33–38.

Iqbal, M.J., Ashiq, M.N., 2007. ’Adsorption of dyes from aqueous solutions on activated charcoal. J. Hazard Mater. 139, 57–66.

Jia, Dongmei, Liu, Min, Xia, Jiangbao, Li, Changhai, 2020. ’Effective removal of aqueous glyphosate using CuFe2O4@biochar derived from phragmites. J. Chem. Technol. Biotechnol. 95, 196–204.

Johnson, Erin R., Keinan, Shahar, Mori-Sánchez, Paula, Contreras-García, Julia, Cohen, Aron J., Yang, Weitao, 2010. ’Revealing noncovalent interactions. J. Am. Chem. Soc. 132, 6498–6506.

Kanissery, Ramdas, Gairhe, Biwek, Kadyampakeni, Davie, Batuman, Ozgur, Alferez, Fernando, 2019. Glyphosate: its environmental persistence and impact on crop health and nutrition’. Plants-Basel 8.

Lalley, J., Han, C., Li, X., Dionysiou, D.D., Nadagouda, M.N., 2016. ’Phosphate adsorption using modified iron oxide-based sorbents in lake water: kinetics, equilibrium, and column tests. Chem. Eng. J. 284, 1386–1396.

Lescano, Maia R., Masin, Carolina E., Rodriguez, Alba R., Godoy, Jose L., Zalazar, Cristina S., 2020. ’Earthworms to improve glyphosate degradation in biobeds. Environ. Sci. Pollut. Control Ser. 27, 27023–27031.

Li, Yajuan, Zhao, Chuanqi, Wen, Yujuan, Wang, Yuanyuan, Yang, Yuesuo, 2018. ’Adsorption performance and mechanism of magnetic reduced graphene oxide in glyphosate contaminated water. Environ. Sci. Pollut. Control Ser. 25, 21036–21048.

Liu, R.T., Chi, L.N., Wang, X.Z., Wang, Y., Sui, Y.M., Xie, T.T., Arandiyan, H., 2019. ’Effective and selective adsorption of phosphate from aqueous solution via trivalent-metals-based amino-MIL-101 MOFs. Chem. Eng. J. 357, 159–168.

Liu, Tong, Cui, Kangping, Chen, Yihan, Li, Chenxuan, Cui, Minshu, Yao, Hongjia, Chen, Yawen, Wang, Shanpeng, 2021. ’Removal of chlorophenols in the aquatic environment by activation of peroxymonosulfate with nMnOx@Biochar hybrid composites: performance and mechanism. Chemosphere 283.

Lu, Tian, Chen, Feiwu, 2012. Multiwfn: a multifunctional wavefunction analyzer. J. Comput. Chem. 33, 580–592.

Lu, Tian, Chen, Qinxue, 2022. Independent gradient model based on Hirshfeld partition: a new method for visual study of interactions in chemical systems. J. Comput. Chem. 43, 539–555.

Lv, Yan-Ran, He, Run-Kai, Chen, Zhuo-Yue, Li, Xin, Xu, Yue-Hua, 2020. ’Fabrication of hierarchical copper sulfide/bismuth tungstate p-n heterojunction with two-dimensional (2D) interfacial coupling for enhanced visible-light photocatalytic degradation of glyphosate. J. Colloid Interface Sci. 560, 293–302.

Mahmoodi, N.M., Ghezelbash, M., Shabanian, M., Aryanasab, F., Saeb, M.R., 2017. ’Efficient removal of cationic dyes from colored wastewaters by dithiocarbamate-functionalized graphene oxide nanosheets: from synthesis to detailed kinetics studies. J. Taiwan Inst. Chem. Eng. 81, 239–246.

Mahmoodi, N.M., Taghizadeh, A., Taghizadeh, M., Azimi, M., 2019. ’Surface modified montmorillonite with cationic surfactants: preparation, characterization, and dye adsorption from aqueous solution. J. Environ. Chem. Eng. 7.

Mesnage, Robin, Antoniou, Michael N., 2017. ’Facts and fallacies in the debate on glyphosate toxicity. Front. Public Health 5.

Möller, Teresia, Paul, Sylvester, 2008. ’Effect of silica and pH on arsenic uptake by resin/iron oxide hybrid media. Water Res. 42, 1760–1766.

National Library of Medicine. USA Viewed on 25-12-2022. National Library of Medicine. https://pubchem.ncbi.nlm.nih.gov/source/hsdb/3432.

Pan, Xuqin, Gu, Zhepei, Chen, Weiming, Li, Qibin, 2021. ’Preparation of Biochar and Biochar Composites and Their Application in a Fenton-like Process for Wastewater Decontamination: A Review. Science of the Total Environment, p. 754.

Persson, Per, Nilsson, Nils, Sjöberg, Staffan, 1996. ’Structure and bonding of orthophosphate ions at the iron oxide–aqueous interface. J. Colloid Interface Sci. 177, 263–275.

Rajabi, M., Mirza, B., Mahanpoor, K., Mirjalili, M., Najafi, F., Moradi, O., Sadegh, H., Shahryari-ghoshekandi, R., Asif, M., Tyagi, I., Agarwal, S., Gupta, V.K., 2016. ’Adsorption of malachite green from aqueous solution by carboxylate group functionalized multi-walled carbon nanotubes: determination of equilibrium and kinetics parameters. J. Ind. Eng. Chem. 34, 130–138.

Saadat, S., Raei, E., Talebbeydokhti, N., 2018. ’Enhanced removal of phosphate from aqueous solutions using a modified sludge derived biochar: comparative study of various modifying cations and RSM based optimization of pyrolysis parameters. J. Environ. Manag. 225, 75–83.

Shang, Y.X., Xu, Q., Gao, Z.X., Li, B.B., Yang, J.S., Wang, Y.F., Peng, Y.Z., 2022. ’Enhanced phosphate removal from practical wastewater via in situ assembled dimension-engineered MOF@carbon heterostructures. Chem. Eng. J. 428.

Singh, Simranjeet, Kumar, Vijay, Singh, Joginder, 2019. Kinetic study of the biodegradation of glyphosate by indigenous soil bacterial isolates in presence of humic acid, Fe(III) and Cu(II) ions. J. Environ. Chem. Eng. 7.

Tan, Ni, Zhao, Yang, Gong, Xiao-bo, Wang, Zhen-ran, Fu, Tao, Liu, Yong, 2019. ’In situ generation of H2O2 using MWCNT-Al/O-2 system and possible application for glyphosate degradation. Sci. Total Environ. 650, 2567–2576.

Wang, Hou, Yuan, Xingzhong, Wu, Yan, Chen, Xiaohong, Leng, Lijian, Wang, Hui, Li, Hui, Zeng, Guangming, 2015. ’Facile synthesis of polypyrrole decorated reduced graphene oxide-Fe3O4 magnetic composites and its application for the Cr(VI) removal. Chem. Eng. J. 262, 597–606.

Wang, Z., Lin, Y., Wu, D.Y., Kong, H.N., 2016. 'Hydrous iron oxide modified diatomite as an active filtration medium for phosphate capture. Chemosphere 144, 1290–1298.

Wang, X.H., Jiang, C.L., Hou, B.X., Wang, Y.Y., Hao, C., Wu, J.B., 2018. 'Carbon composite lignin-based adsorbents for the adsorption of dyes. Chemosphere 206, 587–596.

Wei, Dongning, Li, Bingyu, Huang, Hongli, Luo, Lin, Zhang, Jiachao, Yuan, Yang, Guo, Jiajun, Tang, Lin, Zeng, Guangming, Zhou, Yaoyu, 2018. 'Biochar-based functional materials in the purification of agricultural wastewater: fabrication, application and future research needs. Chemosphere 197, 165–180.

Weng, X.L., Chen, Z.X., Chen, Z.L., Megharaj, M., Naidu, R., 2014. 'Clay supported bimetallic Fe/Ni nanoparticles used for reductive degradation of amoxicillin in aqueous solution: characterization and kinetics. Colloids Surf., A 443, 404–409.

Wu, B.L., Wan, J., Zhang, Y.Y., Pan, B.C., Lo, I.M.C., 2020. 'Selective phosphate removal from water and wastewater using sorption: process fundamentals and removal mechanisms. Environ. Sci. Technol. 54, 50–66.

Xiao, Guqing, Meng, Qiudong, 2020. 'D151 Resin Preloaded with Fe3+ as a Salt Resistant Adsorbent for Glyphosate from Water in the Presence 16% NaCl, vol. 190. Ecotoxicology and Environmental Safety.

Xie, J., Wang, Z., Fang, D., Li, C.J., Wu, D.Y., 2014. 'Green synthesis of a novel hybrid sorbent of zeolite/lanthanum hydroxide and its application in the removal and recovery of phosphate from water. J. Colloid Interface Sci. 423, 13–19.

Xie, Qiying, Li, Yan, Lv, Zhaoling, Zhou, Hang, Yang, Xiangjun, Chen, Jing, Guo, Hong, 2017. 'Effective adsorption and removal of phosphate from aqueous solutions and eutrophic water by Fe-based MOFs of MIL-101. Sci. Rep. 7.

Yamaguchi, Natalia Ueda, Bergamasco, Rosangela, Hamoudi, Safia, 2016. 'Magnetic MnFe2O4-graphene hybrid composite for efficient removal of glyphosate from water. Chem. Eng. J. 295, 391–402.

Yantasee, W., Lin, Y.H., Alford, K.L., Busche, B.J., Fryxell, G.E., Engelhard, M.H., 2004. 'Electrophilic aromatic substitutions of amine and sulfonate onto fine-grained activated carbon for aqueous-phase metal ion removal. Separ. Sci. Technol. 39, 3263–3279.

Zhan, Hui, Feng, Yanmei, Fan, Xinghui, Chen, Shaohua, 2018. Recent advances in glyphosate biodegradation. Appl. Microbiol. Biotechnol. 102, 5033–5043.

Zhang, Chen, Cui, Lai, Zeng, Guangming, Huang, Danlian, Yang, Chunping, Wang, Yang, Zhou, Yaoyu, Cheng, Min, 2016. Efficacy of carbonaceous nanocomposites for sorbing ionizable antibiotic sulfamethazine from aqueous solution. Water Res. 95, 103–112.

Zhao, F.P., Tang, W.Z., Zhao, D.B., Meng, Y., Yin, D.L., Sillanpaa, M., 2014. 'Adsorption kinetics, isotherms and mechanisms of Cd(II), Pb(II), Co(II) and Ni(II) by a modified magnetic polyacrylamide microcomposite adsorbent. J. Water Process Eng. 4, 47–57.

Zhao, X., Jin, H., Chen, Y.N., Ge, Z.W., 2021. 'Numerical study of H-2, CH4, CO, O-2 and CO2 diffusion in water near the critical point with molecular dynamics simulation. Comput. Math. Appl. 81, 759–771.

Zheng, Yan, Zheng, Shasha, Xue, Huaiguo, Pang, Huan, 2018. 'Metal-Organic frameworks/graphene-based materials: preparations and applications. Adv. Funct. Mater. 28.

Zhong, Guihao, Liu, Dingxin, Zhang, Jianyong, 2018. 'Incorporation of functional groups expands the applications of UiO-67 for adsorption, catalysis and thiols detection. ChemistrySelect 3, 7066–7080.

Zhou, Y.M., Gao, B., Zimmerman, A.R., Chen, H., Zhang, M., Cao, X.D., 2014. 'Biochar-supported zerovalent iron for removal of various contaminants from aqueous solutions. Bioresour. Technol. 152, 538–542.